



Mechanochemical Synthesis of Fluorine-Containing Co-Doped Zeolitic Imidazolate Frameworks for Producing Electrocatalysts

Max Rautenberg^{1,2}, Marius Gernhard³, Jörg Radnik¹, Julia Witt¹, Christina Roth³ and Franziska Emmerling^{1,2*}

¹BAM Federal Institute of Materials Research and Testing, Berlin, Germany, ²Department of Chemistry, Humboldt-Universität zu Berlin, Berlin, Germany, ³Fakultät für Ingenieurwissenschaften, Lehrstuhl für Werkstoffverfahrenstechnik, Universität Bayreuth, Bayreuth, Germany

OPEN ACCESS

Edited by:

Elena Vladimirovna Boldyreva,
Novosibirsk State University, Russia

Reviewed by:

Yinlong Zhu,
Monash University, Australia
Lujia (Luke) Liu, Victoria University of
Wellington, New Zealand
Maria Teresa Duarte,
Universidade de Lisboa, Portugal

*Correspondence:

Franziska Emmerling
franziska.emmerling@bam.de

Specialty section:

This article was submitted to
Solid State Chemistry,
a section of the journal
Frontiers in Chemistry

Received: 21 December 2021

Accepted: 24 January 2022

Published: 14 March 2022

Citation:

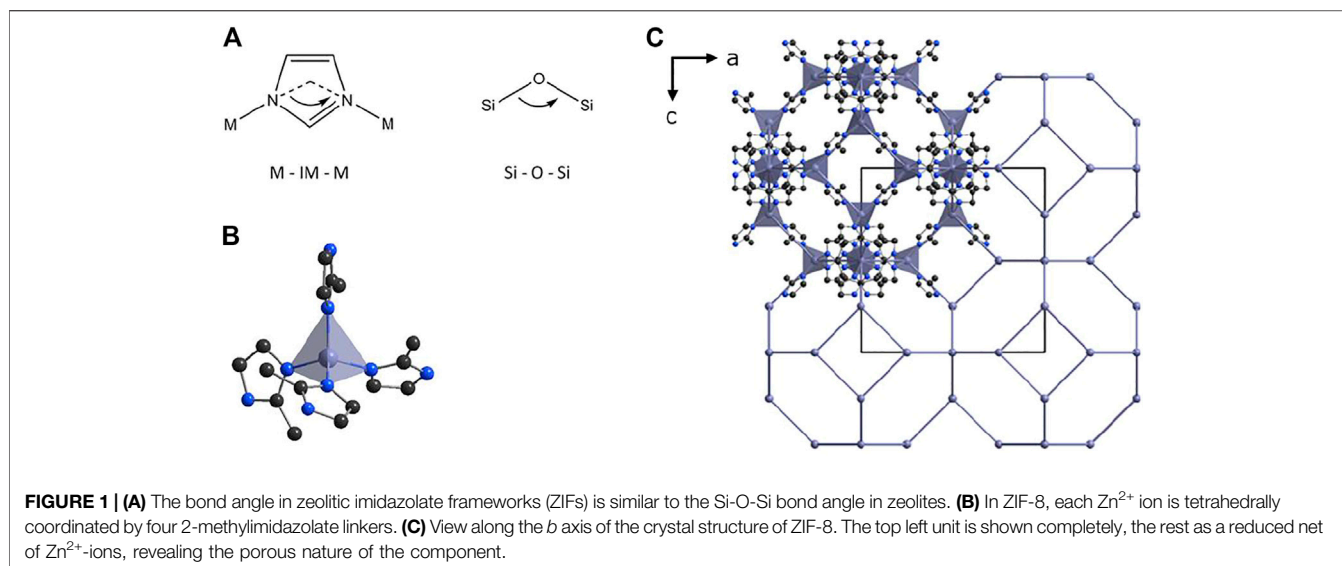
Rautenberg M, Gernhard M, Radnik J,
Witt J, Roth C and Emmerling F (2022)
Mechanochemical Synthesis of
Fluorine-Containing Co-Doped Zeolitic
Imidazolate Frameworks for
Producing Electrocatalysts.
Front. Chem. 10:840758.
doi: 10.3389/fchem.2022.840758

Catalysts derived from pyrolysis of metal organic frameworks (MOFs) are promising candidates to replace expensive and scarce platinum-based electrocatalysts commonly used in polymer electrolyte membrane fuel cells. MOFs contain ordered connections between metal centers and organic ligands. They can be pyrolyzed into metal- and nitrogen-doped carbons, which show electrocatalytic activity toward the oxygen reduction reaction (ORR). Furthermore, metal-free heteroatom-doped carbons, such as N-F-Cs, are known for being active as well. Thus, a carbon material with Co-N-F doping could possibly be even more promising as ORR electrocatalyst. Herein, we report the mechanochemical synthesis of two polymorphs of a zeolitic imidazole framework, Co-doped zinc 2-trifluoromethyl-1H-imidazolate ($Zn_{0.9}Co_{0.1}(CF_3\text{-Im})_2$). Time-resolved *in situ* X-ray diffraction studies of the mechanochemical formation revealed a direct conversion of starting materials to the products. Both polymorphs of $Zn_{0.9}Co_{0.1}(CF_3\text{-Im})_2$ were pyrolyzed, yielding Co-N-F containing carbons, which are active toward electrochemical ORR.

Keywords: MOF (Metal–Organic framework), mechanochemistry, XRD, electrocatalysis, mixed metal

INTRODUCTION

Polymer membrane fuel cells (PMFCs) are of significant interest as a device for clean energy conversion. Their broad commercial application is currently limited by the inefficient oxygen reduction reaction (ORR). The slow kinetics of the ORR makes catalysis essential. State-of-the-art catalyst are currently based on platinum group metals (Gasteiger et al., 2005; Wu and Yang, 2013; Evers et al., 2019; Jiang et al., 2021; Zhang et al., 2021), but with their high price and scarcity, they limit a large-scale application. Therefore, low-cost and readily available alternatives are sought for. Reportedly, metal and nitrogen doped carbons (M-N-Cs) show high ORR activity, following the order $M = Fe > Co > Mn > Cu \gg Ni$ (Masa et al., 2014; Peng et al., 2014). The origin of the catalytic activity is speculated as M-N₄ centers (M = Fe, Co) in a graphene matrix. However, Fe-based catalysts tend to produce Fe^{2+/3+} that can react with the ORR possible byproduct H₂O₂ generating hydroxyl and hydroperoxyl radical species. This mixture, known as Fenton's reagent (Kang and Chang, 1997; Walling, 2002), can decompose organic matter, such as the proton conducting membrane of PMFCs. Alternatively, Co-based catalysts, showing similar performance as Fe-based catalysts without the risk of Fenton's reaction, can be used.



Zeolitic imidazole frameworks (ZIFs) (Park et al., 2006), a class of metal organic frameworks (MOFs), consisting of metal nodes, linked by imidazole-based linkers can serve as templates, which can be converted in to M-N-C ORR catalysts by pyrolysis. ZIF materials are commonly used for gas storage (Eddaoudi et al., 2002) and separation (Keskin et al., 2010), oil spill cleaning (Mondal et al., 2017), catalysis (Farrusseng et al., 2009; Hu et al., 2020), sensing (Chapartegui-Arias et al., 2019; Zhang et al., 2020), and drug delivery (Hao et al., 2021; Ibrahim et al., 2017; Nirosha Yalamandala et al., 2021), as precursors for electrocatalysis (Li et al., 2016; Wang et al., 2014; Zhao et al., 2014) and as stimuli-responsive materials (Iacomini and Maurin, 2021). The crystal structures of these porous coordination polymers are based on the topology nets of zeolites. Furthermore, the metal-imidazolate-metal bond angles in ZIFs resemble the Si-O-Si bond angles in zeolites, as well as the tetrahedral coordination of metal centers by imidazolate ligands (Figures 1A,B). ZIFs have a broad variety of possible structures, depending on how the metal-imidazolate-tetrahedrons are interconnected (Schröder et al., 2013). In the well-studied compound ZIF-8, where zinc is tetrahedrally coordinated by 2-methylimidazolate linkers, the tetrahedral units form sodalite cages (SOD) (Figure 1C), resulting in a porous material (Park et al., 2006). Other ZIFs can form dense topologies, which resemble α -quartz (qtz).

Ma et al. showed that Co-based ZIFs can be easily pyrolyzed into Co-N-C catalysts for ORR by pyrolysis. (Ma et al., 2011). The resulting catalysts show high activity in alkaline media (Chao et al., 2015; Chen et al., 2015; Wang et al., 2016) but lower activity under acid conditions (Wang et al., 2014; You et al., 2015). Direct pyrolysis of cobalt 2-methylimidazolate (ZIF-67) leads to a porous carbon material with aggregated cobalt nanoparticles, resulting in a loss of active Co-N₄ species and therefore ORR activity (Ma et al., 2011; Xia et al., 2014; Wang et al., 2016). Using zinc-based ZIFs with low amounts of cobalt results in a porous carbon material with uniformly distributed Co-N₄ sites and no metallic cobalt particles, showing excellent ORR activity (Wang et al., 2016). Furthermore, doping of carbons with heteroatoms can yield ORR active materials. In case of N-, F-doping, a

cooperative N and F polarization of carbon is speculated as the mechanism (Lv et al., 2017).

Different synthesis routes were established for ZIFs, including microwave-assisted (Bux et al., 2009), sonochemical (Son et al., 2008; Yang et al., 2012), electrochemical (Martinez Joaristi et al., 2012) and solvothermal methods (Palaniselvam et al., 2013), or crystal growth from solution (Venna et al., 2010). Most of these methods involve solvents such as N,N-dimethylformamide, N,N-diethylformamide, or methanol (Huang et al., 2006; Park et al., 2006; Cravillon et al., 2009; Kukkar et al., 2021). Mechanochemistry, as an alternative green and solvent-free method, has been established for several MOF synthesis including ZIF-8 (Pichon et al., 2006; Klimakow et al., 2010; Batzdorf et al., 2015; Chen et al., 2019; Szczęśniak et al., 2020).

Here, we present the mechanochemical synthesis of fluorine-substituted ZIF-8 frameworks including Co-doping. We figured a Co-doped $\text{Zn}(\text{CF}_3\text{-Im})_2$ could be a promising precursor for a highly active ORR catalysts, combining positive effects of both CoN₄-clusters and N-F-doping.

The samples were thoroughly characterized by X-ray diffraction (XRD), nitrogen sorption, transmission electron microscopy (TEM), and energy-dispersive X-ray spectroscopy (EDX). Furthermore, the formation process in the ball mill was followed by time-resolved *in situ* synchrotron XRD, gaining insights in the formation process of the compounds. The two polymorphs of $\text{Zn}_{0.9}\text{Co}_{0.1}(\text{CF}_3\text{-Im})_2$ were pyrolyzed, and the carbonous materials' chemical composition was analyzed by X-ray photoelectron spectroscopy (XPS). Furthermore, both pyrolyzed qtz- and SOD- $\text{Zn}_{0.9}\text{Co}_{0.1}(\text{CF}_3\text{-Im})_2$ were shown to be active toward ORR.

EXPERIMENTAL SECTION

Materials

The following chemicals were used: zinc oxide (ZnO, ACS reagent; Acros Organics, USA), 2-methylimidazole $\text{C}_4\text{H}_6\text{N}_2$ ($\geq 98\%$; Sigma-Aldrich, Germany), cobalt (II) acetate tetrahydrate ($\text{Co}(\text{CH}_3\text{COO})_2 \cdot 4 \text{H}_2\text{O}$; Baker analyzed, J. T. Baker, USA), zinc

acetate ($\text{Zn}(\text{CH}_3\text{COO})_2 \cdot 2 \text{H}_2\text{O}$; >98% ACS Reagent, Fluka; Honeywell International Inc.), basic zinc carbonate $\text{Zn}_5(\text{CO}_3)_2(\text{OH})_6$ (>97%, Thermo Fisher Scientific, USA), 2-trifluoromethyl-1H-imidazole $\text{C}_4\text{H}_3\text{N}_2\text{F}_3$ (>95%; Fluorochem, United Kingdom), potassium hydroxide KOH (Sigma-Aldrich), perchloric acid HClO_4 (Bernd Kraft, Germany) and isopropanol (Sigma-Aldrich). Nafion was purchased from Sigma-Aldrich. All chemicals were used without further purification.

Synthesis of ZIF-8 and $\text{Zn}_{0.9}\text{Co}_{0.1}(\text{2Me-Im})_2$

Zinc oxide (0.337 mmol, 27.4 mg), zinc acetate dihydrate (10 mol% of total metal content, 0.037 mmol, 8.2 mg), 2-methylimidazole (0.748 mmol, 61.4 mg), and NH_4NO_3 (0.748 mmol, 3.0 mg) were placed into a custom-made milling jar (PMMA, 5 mL) (Lampronti et al., 2021). After adding one stainless-steel milling ball (7-mm diameter) and methanol (15 μL), the jar was closed and mounted into a vertical ball mill (Pulverisette 23; Fritsch GmbH, Idar-Oberstein, Germany). The mixture was ground for 15 min at a frequency of 50 Hz. The product was obtained as a white voluminous powder.

For Co-doping, the zinc acetate dihydrate was replaced by cobalt acetate tetrahydrate (10 mol% of total metal content, 0.037 mmol, 9.2 mg), which was added to the milling jar (PMMA, 5 mL), along with ZnO (0.333 mmol, 27.1 mg), 2-methylimidazole (0.740 mmol, 60.7 mg), NH_4NO_3 (0.037 mmol, 3.0 mg), methanol (15 μL), and a stainless-steel grinding ball (7-mm diameter). The mixture is ground for 15 min at a frequency of 50 Hz, and a purple voluminous powder is obtained.

Synthesis of $\text{qtz-Zn}(\text{CF}_3\text{-Im})_2$ and $\text{qtz-Zn}_{0.9}\text{Co}_{0.1}(\text{CF}_3\text{-Im})_2$

In a typical experiment, hydrozincite ($\text{Zn}_5(\text{CO}_3)_2(\text{OH})_6$, 0.052 mmol, 28.8 mg) and 2-trifluoromethyl-1H-imidazole (0.524 mmol, 71.3 mg) are weighed out and alongside a stainless-steel milling ball (7-mm diameter) are placed into a custom-made milling jar (PMMA, 5 mL). After adding methanol (15 μL), the jar was closed and mounted into a vertical ball mill (Pulverisette 23; Fritsch GmbH). The mixture was ground at a frequency of 50 Hz for 15 min. The product was obtained as a yellow-brown powder.

For Co-doping, the desired molar percentage of metal is replaced by cobalt acetate tetrahydrate. In a typical experiment with 10 mol% Co-doping, hydrozincite ($\text{Zn}_5(\text{CO}_3)_2(\text{OH})_6$, 0.046 mmol, 25.0 mg), cobalt acetate tetrahydrate (10 mol% relative to total metal amount, 0.025 mmol, 6.2 mg), and 2-trifluoromethyl-1H-imidazole (0.505 mmol, 68.7 mg) are weighed out and placed into a custom-made milling jar (PMMA, 5 mL). After adding one stainless steel milling ball (7-mm diameter), the jar is closed and mounted into a (Pulverisette 23; Fritsch GmbH) vertical ball mill. The mixture was ground for 15 min at a frequency of 50 Hz. The product was obtained as a purple-brown powder.

Synthesis of $\text{SOD-Zn}(\text{CF}_3\text{-Im})_2$ and $\text{SOD-Zn}_{0.9}\text{Co}_{0.1}(\text{CF}_3\text{-Im})_2$

To obtain $\text{SOD-Zn}(\text{CF}_3\text{-Im})_2$ the reactant masses are kept constant ($\text{Zn}_5(\text{CO}_3)_2(\text{OH})_6$: 0.052 mmol, 28.8 mg; 2-trifluoromethyl-1H-imidazole: 0.524 mmol, 71.3 mg), one

stainless-steel milling ball (5-mm diameter) and DMF (20 μL) were used. The mixture was ground for 7 min at 50 Hz, and a damp brown powder was obtained. After completely drying the powder, it is washed three times with methanol (20 mL) and air dried.

$\text{Zn}_{0.9}\text{Co}_{0.1}(\text{CF}_3\text{-Im})_2$ can be obtained when $\text{Zn}_5(\text{CO}_3)_2(\text{OH})_6$ (0.046 mmol, 25.0 mg), cobalt acetate tetrahydrate (0.025 mmol, 6.3 mg), and 2-trifluoromethyl-1H-imidazole (0.505 mmol, 68.8 mg) are placed alongside a single grinding ball (5-mm diameter, stainless steel) into a custom-made milling jar (PMMA, 5 mL). The mixture is ground at 50 Hz for 8 min, yielding a damp purple-brown solid. After drying at air, the solid is finely ground in a mortar and washed with methanol (20 mL) three times and then dried at air.

Preparation of Electrocatalysts

To prepare the electrocatalysts, the carbonous residue after carbonization was loaded on glassy carbon (GC) rotating disk electrode (RDE) according to the procedure described by Kocha et al. (2017). The method involved initial preparation of a stock solution with 10 mL isopropanol (Sigma-Aldrich), 0.2 mL of 5 wt% Nafion ionomer solution (Sigma-Aldrich) and 39.8 mL of deionized water (0.055 $\mu\text{S}/\text{cm}$, Evoqua, United States). To prepare catalytic inks from the powder samples, 1.3 mg of the compound was mixed with 1 mL of the stock solution. The inks were homogenized for 45 min in an ultrasonic bath at 80 Hz. Afterward, the dispersion (10 μL) was deposited on a clean GC electrode and spun at 900 revolutions/min (rpm) until the liquid was evaporated.

Electrochemical characterizations of the heterogeneous catalyst powders were conducted using a three-electrode setup with a Gamry Reference 600 + potentiostat (Gamry Instruments, United States). Before each measurement, the electrolyte was degassed for 30 min with nitrogen and oxygen, respectively. All measurements were performed in 0.1 M KOH or in 0.1 M HClO_4 by using a Pt counter electrode and an Ag/AgCl (3 M NaCl) reference electrode. Linear sweep voltammetry experiments were performed in a potential range of +1.1 V to -0.3 V in acidic media and +0.5 V to -0.8 V in alkaline media at a scan rate of 20 mV s^{-1} , whereas the RDE was operated at rotation speeds of 600, 900, and 1,600 rpm. All potentials were reported with respect to the standard hydrogen electrode (SHE). The surface area of the GC electrode was 0.126 cm^2 . Prior to use, the GC electrode was polished with 0.3 and 0.05 mm alumina powder followed by sonicating and rinsing with deionized water after each polishing step for 5 min to remove the alumina and abraded particles.

Powder XRD

Powder XRD data were collected using a Bruker D8 Advance diffractometer (Bruker AXS, Germany) in Bragg-Brentano-Geometry with a Lynxeye-detector using Cu-K_α radiation ($\lambda = 1.542 \text{ \AA}$) over a range of $2\theta = 5^\circ - 60^\circ$ with a step size of 0.02° . The time per step was 0.6 s. The finely ground dried sample was packed onto a standard PVC sample holder, which was mounted into the diffractometer.

Synchrotron XRD

The *in situ* XRD experiments were performed at the μ Spot beamline (BESSY II, Helmholtz Centre Berlin for Materials and Energy). The used beam diameter was 100 μ m at a photon energy of 16.576 keV using a double crystal monochromator (Si 111). To minimize double reflections, the beam was positioned inside of the milling jar, by scanning the wall of the jar and then moving approximately 50 μ m inside. The sample detector distance was 229.70 mm. Scattered intensities were collected with a two-dimensional X-ray detector (Eiger 9M, HPC 3,110 \times 3,269 pixels, pixel size 75 \times 75 μ m) and a time-resolution of 30 s. The obtained scattering images were processed using an algorithm of the computer program DPDAK (Benecke et al., 2014). The resulting patterns (q/nm^{-1} vs. intensity/a.u.) were analyzed, processed, and plotted using Origin (Version 2020; OriginLabs Corporation, Northampton, MA, United States). For comparison, the theoretical XRD patterns of the starting materials and final products were retrieved from crystallographic databases ICSD or CCDC and simulated using Mercury (version 4.3.0, CCDC) (Macrae et al., 2020). All XRD plots are background corrected by a custom-made python script.

Differential Scanning Calorimetry–TGA

Thermogravimetric analysis (TGA) and differential scanning calorimetry (DSC) was performed simultaneously on dry powders (~10 mg) using a heat flux TGA-DSC 3+ (Mettler-Toledo). All measurements were carried out under a continuous nitrogen flow of 10 mL/min. As a reference, an empty α -Al₂O₃ corundum crucible was used. The samples were heated with a heating rate of 10 K/min from room temperature to 900°C and held for 1 h. Subsequently, the samples were allowed to cool down under continuous nitrogen gas flow.

X-Ray Photoelectron Spectroscopy

All measurements were performed with an AXIS Ultra DLD photoelectron spectrometer manufactured by Kratos Analytical (Manchester, United Kingdom). XPS spectra were recorded using monochromatized aluminum K α radiation for excitation, at a pressure of approximately 5 \times 10⁻⁹ mbar. The electron emission angle was 0°, and the source-to-analyzer angle was 60°. The binding energy scale of the instrument was calibrated following a Kratos Analytical procedure, which uses ISO 15472 binding energy data. Spectra were taken by setting the instrument to the hybrid lens mode and the slot mode providing approximately a 300 \times 700- μ m² analysis area. Furthermore, the charge neutralizer was used. Survey spectra were recorded with a step size of 1 eV and a pass energy of 80 eV; high-resolution spectra were recorded with a step size of 0.1 eV and a pass energy of 20 eV. Quantification was performed with Unifit 2021 using Scofield factor, the inelastic mean free pathway, and the transmission function for the normalization of the peak area. For peak fitting, a sum Gaussian–Lorentzian function was used. As background, a modified Tougaard background was used. Measurement uncertainties are \pm 0.2 eV with a confidence interval of 95% for binding energies at high-resolution spectra.

Elemental quantification has a relative uncertainty of \pm 20% with a confidence interval of 95%.

Transmission electron microscopy and Energy dispersive X-Ray Spectroscopy

TEM images were obtained in a Talos F200S Microscope (Thermo Fisher Scientific) by using a 200-kV microscopy technique in which a beam of electrons is transmitted through a specimen to form an image. The specimens were prepared by dropping sample solutions (1 mg/mL in water/solvent) onto a 3-mm copper grid (lacey, 400 mesh) and leaving them to air-dry at room temperature. To determine the elemental composition of the ZIF-8 and Zn_{0.9}Co_{0.1} (2Me-Im)₂ specimen, EDX with two silicon drift detectors (SDD) was used. Counting time for X-ray spectra was 60 s.

Gas Sorption

Nitrogen gas sorption at 77 K was performed on an ASAP 2020 (Micrometrics) and was used to calculate the specific surface area from a multipoint adsorption isotherm with the BET (Brunauer–Emmit–Teller) calculation model (relative pressure range, 0.0012–0.0298) according to DIN ISO 9277:2014 (Brunauer et al., 1938).

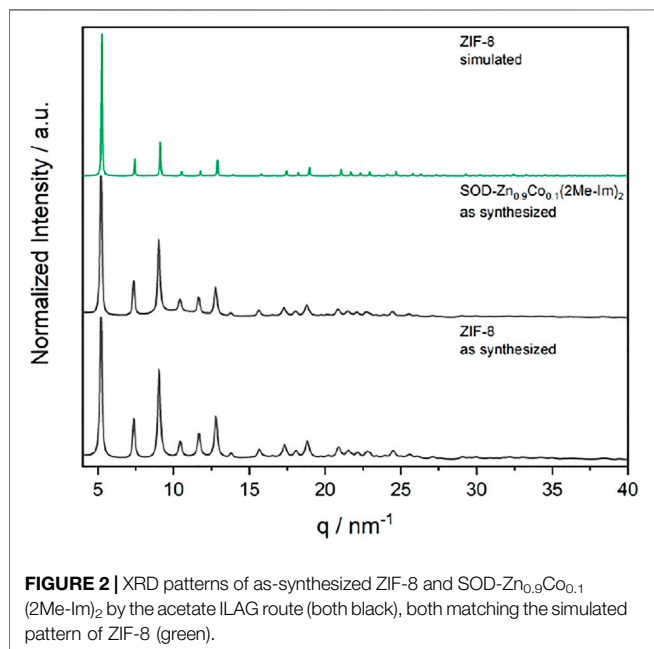
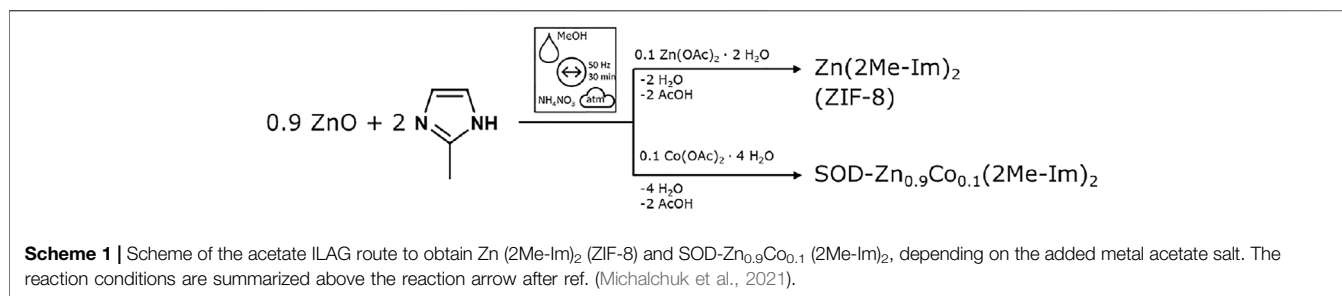
RESULTS AND DISCUSSION

Co-Doping of ZIF-8 by Acetate Ionic and Liquid-Assisted Grinding Route

Scheme 1 details the synthesis strategy to obtain ZIF-8 and SOD-Zn_{0.9}Co_{0.1} (2Me-Im)₂. We used a modified synthesis combining ionic and liquid-assisted grinding (ILAG) conditions (Frišćić et al., 2010) and an acetate route described by Imawaka et al. (2019), Tanaka et al. (2017). Both ZIF-8 and SOD-Zn_{0.9}Co_{0.1} (2Me-Im)₂ were obtained phase pure and identified by XRD (**Figure 2**). All synthesis procedures were analyzed *via* time-resolved *in situ* XRD to analyze the reaction mechanism and potential phase transformations. These reactions were performed in a custom-built PMMA milling jar (Lampronti et al., 2021).

The SOD-Zn_{0.9}Co_{0.1} (2Me-Im)₂ powder was examined by TEM (**Supplementary Figure S1**) and EDX to assess its elemental composition. The Co content of 7.85% is close to the expected value of 10% of total metal content. Together with the XRD results, these data indicate the successful introduction of cobalt into the parental ZIF-8 structure (**Supplementary Figure S2**). Furthermore, the surface area of ZIF-8 and SOD-Zn_{0.9}Co_{0.1} (2Me-Im)₂ powders synthesized by the acetate ILAG route was studied after an activation protocol by nitrogen sorption at 77 K using the Brunauer–Emmett–Teller theory (**Supplementary Figure S3**). The samples exhibited type I isotherms with BET-surface areas of 1,695 m²/g (ZIF-8) and 1,554 m²/g (SOD-Zn_{0.9}Co_{0.1} (2Me-Im)₂), which are comparable to literature reports (Park et al., 2006; Kaur et al., 2016).

The synthesis of the ZIF structures was investigated by time-resolved *in situ* XRD. In agreement with previous *in situ* studies,



the parent structure ZIF-8 formation proceeds rapidly indicated by the appearance of first ZIF-8 reflections after 30 s (Batzdorf et al., 2015). The ZnO reflections gradually decrease until disappearing completely after 7 min, leaving ZIF-8 as the single product phase. Continued milling does not change the composition and crystallite size (Supplementary Figure S4). For SOD-Zn_{0.9}Co_{0.1}(2Me-Im)₂, the time-resolved *in situ* XRD data (Figure 3) follow a comparable mechanism, with slightly different detection phases of the reactant (cobalt acetate tetrahydrate visible until 30 s and zinc oxide until approximately 6 min). The data suggest that the formation of SOD-Zn_{0.9}Co_{0.1}(2Me-Im)₂ starts within the first 20 s and continues until it reaches completion after approximately 3 min.

Zn(CF₃-Im)₂ by Ball Mill Grinding; Polymorphic Control by Choice of Grinding Liquid.

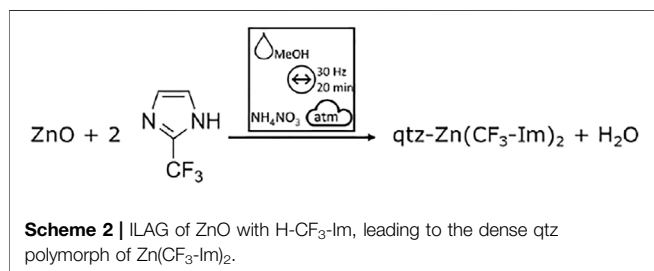
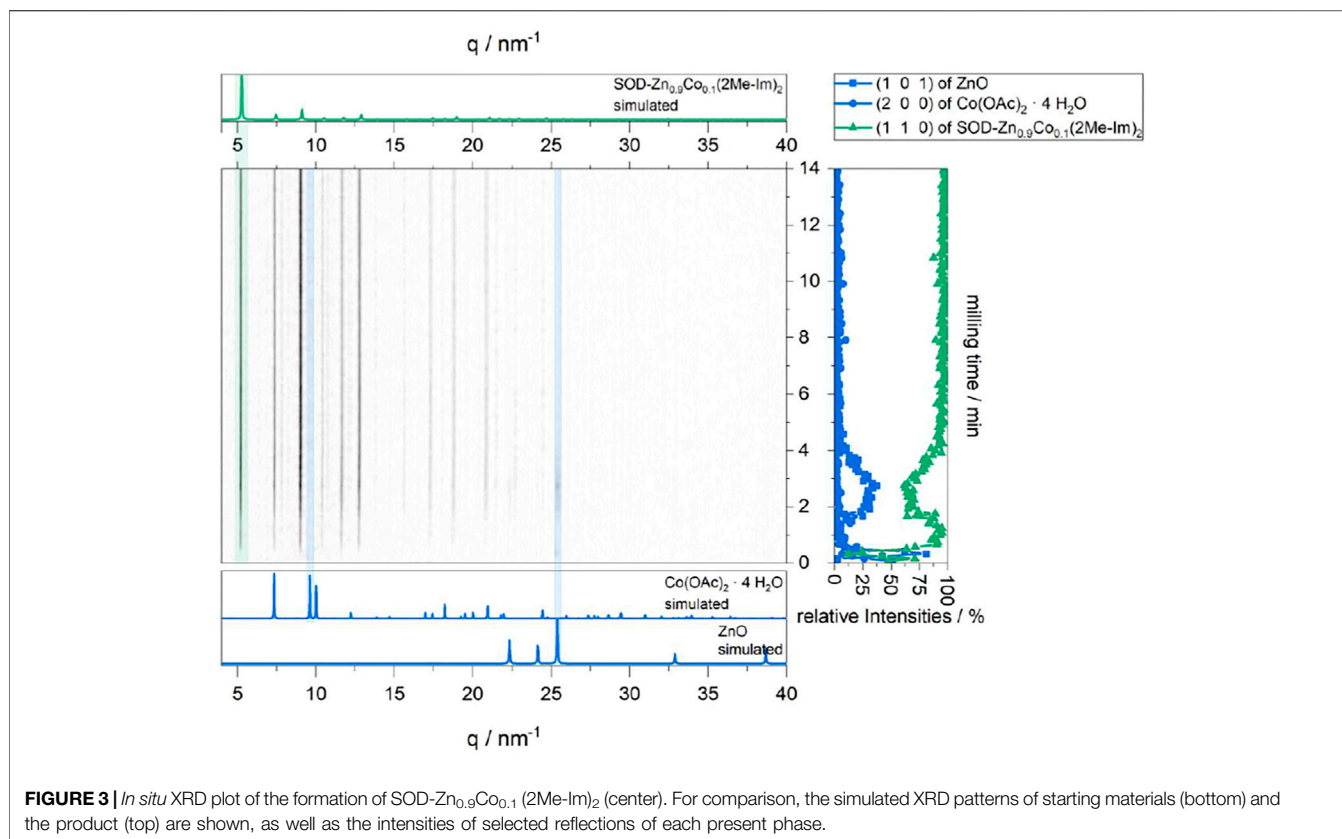
Fluorinated MOFs are of great interest because of their improved properties compared with their nonfluorinated counterparts. The increased hydrophobicity raises the performance in gas separation (Mondal et al., 2017; Cheplakova et al., 2018), gas

storage (Zhang et al., 2013), or in the cleanup of oil spillages (Yang et al., 2011). Metal-free carbon materials with heteroatom-doping (F, N) show electrocatalytic ORR activity (Lv et al., 2017). Furthermore, with higher hydrophobicity in an ORR catalyst prepared from a fluorinated ZIF, we would expect a more efficient transport of water away from the active oxygen reduction site, resulting in improved kinetics for the ORR. Therefore, Zn(CF₃-Im)₂ was chosen as fluorinated analog to ZIF-8 and as a host material for Co-doping. As Zn(CF₃-Im)₂ can crystallize in two polymorphic crystal structures (Arhangel'skis et al., 2019), the goal was to prepare both the quartz (qtz) and sodalite (SOD) topologies of the material, as well as achieving Co-doping in both of them (Schröder et al., 2013).

The synthesis of the dense qtz-Zn(CF₃-Im)₂ polymorph was easily achieved by ILAG of zinc oxide and H-CF₃-Im, using NH₄NO₃ and methanol (Scheme 2), which is in good agreement with the literature (Arhangel'skis et al., 2019). The preparation of SOD-Zn(CF₃-Im)₂ by ILAG from zinc oxide as a starting material seems not straightforward, as SOD-Zn(CF₃-Im)₂ is an intermediate in the formation of qtz-Zn(CF₃-Im)₂. As opposed to the literature, the ethanol assisted grinding of Zn₅(CO₃)₂(OH)₆ with H-CF₃-Im did not yield phase pure SOD-Zn(CF₃-Im)₂, but a mixture of the qtz and SOD polymorphs. The mechanochemical Zn(CF₃-Im)₂ formation by MeOH-assisted grinding of Zn₅(CO₃)₂(OH)₆ with H-CF₃-Im was studied by time-resolved *in situ* XRD. After a short induction period (0–1 min), an interval with no detectable diffraction signals (1–5 min) is observed. From 5 min on the (100) and (101), reflections of qtz-Zn(CF₃-Im)₂ are detectable. The intensity of these reflections increases, and further reflections of qtz-Zn(CF₃-Im)₂ appear. Against our preliminary results and literature records (Arhangel'skis et al., 2019), no intermediate phase of SOD-Zn(CF₃-Im)₂ was found. Instead, a direct conversion of starting materials into qtz-Zn(CF₃-Im)₂ can be observed (Supplementary Figure S5).

The *in situ* data show that under the chosen milling conditions, the reaction mechanism does not include the formation of the SOD polymorph. In a parameter study, varying milling frequency (15, 30, 50 Hz), milling ball size (3, 5, 7 mm), and added grinding liquid (MeOH, EtOH, DMF), we identified the milling conditions for the porous SOD polymorph. DMF-assisted grinding with a single 5-mm steel ball at 50 Hz yielded the SOD-Zn(CF₃-Im)₂, whereas MeOH ILAG leads to qtz-Zn(CF₃-Im)₂ (Figure 4). The milling conditions leading to both polymorphs are summarized in Scheme 3.

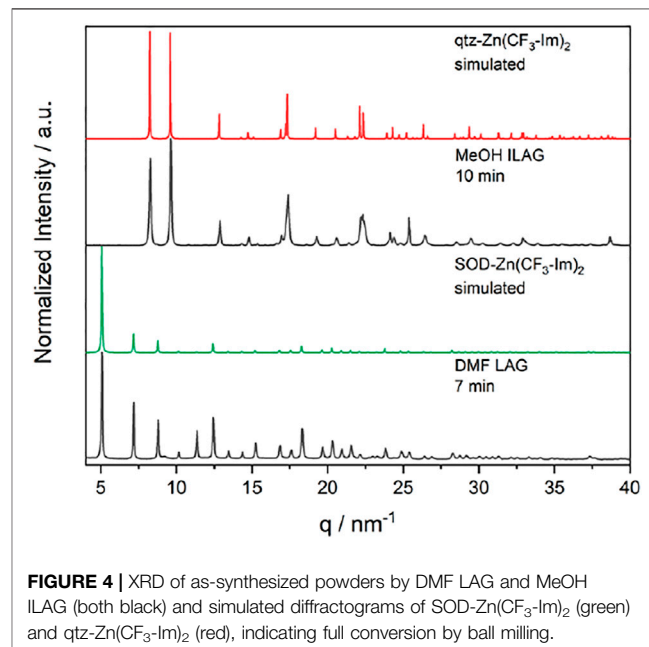
The mechanochemical synthesis of SOD-Zn(CF₃-Im)₂ was monitored by *in situ* XRD to gain insights in the formation



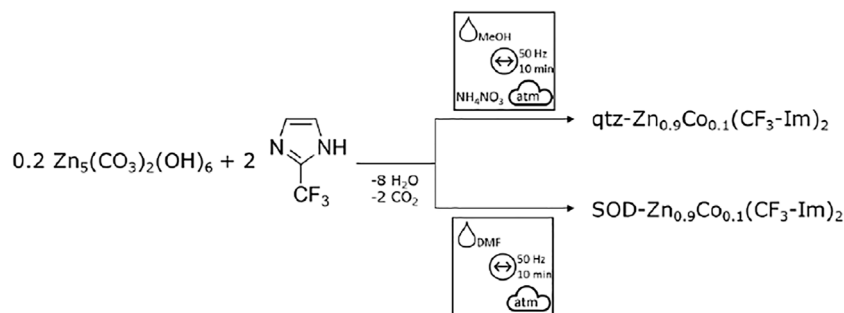
process. The *in situ* plot shows the one-step formation of SOD-Zn(CF₃-Im)₂ under LAG with DMF (**Supplementary Figure S6**). The intensity of starting materials reflections ((200) of Zn₅(CO₃)₂(OH)₆ and (021) of H-CF₃-Im) decreases over time, with increasing intensity of the (110) reflection of the SOD polymorph of Zn(CF₃-Im)₂. After approximately 6 min, the intensities of the present phases reach a plateau with little variance, correlating to the sample amount in the beam. Moreover, no conversion of the SOD polymorph into the qtz polymorph can be observed within the observed time frame.

Co-Doping of Zn(CF₃-Im)₂ by Acetate ILAG/LAG Route

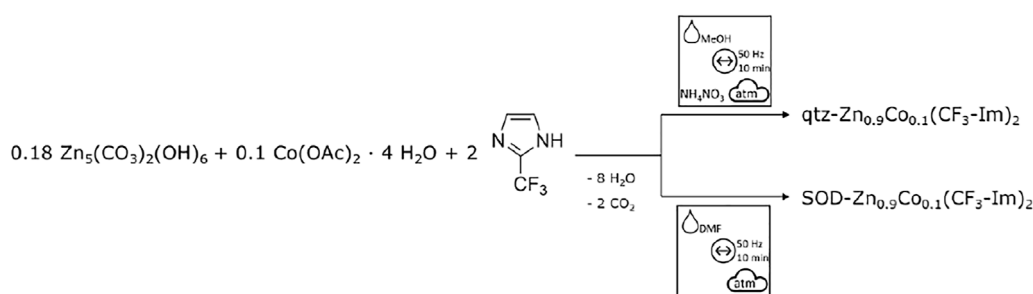
To achieve Co-doping into the Zn(CF₃-Im)₂, we modified the synthesis, replacing 10 mol% of the total metal amount with



cobalt acetate tetrahydrate, while keeping the milling conditions of the undoped -Zn(CF₃-Im)₂ (**Scheme 4**). Both polymorphs of Zn(CF₃-Im)₂ were successfully prepared by the herein presented route, in 100-mg as well as 1-g scale (**Figure 5**).



Scheme 3 | Synthesis scheme of both polymorphs of $\text{Zn}(\text{CF}_3\text{-Im})_2$. Depending on the grinding conditions the product can be obtained as dense qtz- or porous SOD polymorph.



Scheme 4 | Modified synthesis route for Co-doping of both polymorphs of $\text{Zn}_{0.9}\text{Co}_{0.1}(\text{CF}_3\text{-Im})_2$ by ball mill grinding.

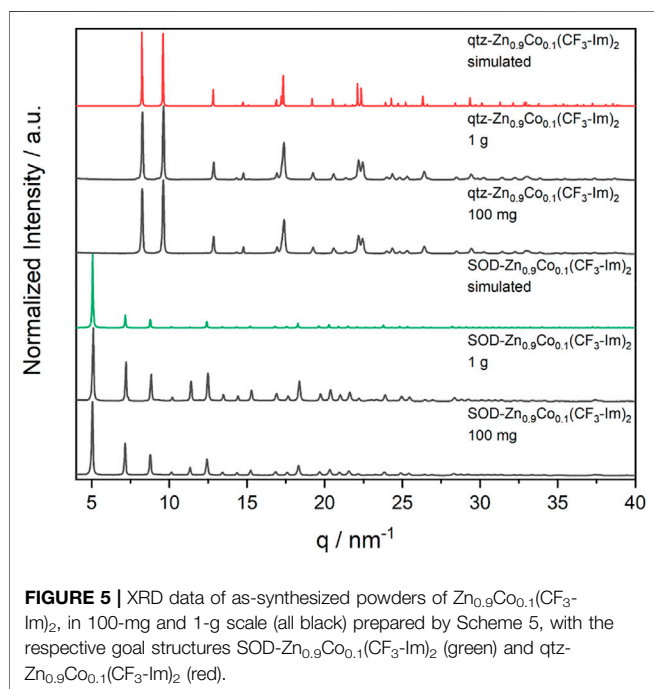


FIGURE 5 | XRD data of as-synthesized powders of $\text{Zn}_{0.9}\text{Co}_{0.1}(\text{CF}_3\text{-Im})_2$, in 100-mg and 1-g scale (all black) prepared by Scheme 5, with the respective goal structures SOD- $\text{Zn}_{0.9}\text{Co}_{0.1}(\text{CF}_3\text{-Im})_2$ (green) and qtz- $\text{Zn}_{0.9}\text{Co}_{0.1}(\text{CF}_3\text{-Im})_2$ (red).

XRD was also performed for the MeOH-ILAG route to qtz- $\text{Zn}_{0.9}\text{Co}_{0.1}(\text{CF}_3\text{-Im})_2$. The data in **Figure 6** can be divided into several phases. In the first phase until 1 min, the intensity of

starting material rises, due to more powder being in the beam. Furthermore, the (110) reflection of SOD- $\text{Zn}_{0.9}\text{Co}_{0.1}(\text{CF}_3\text{-Im})_2$ appears but stays weak. Afterward, the intensity of starting materials and SOD- $\text{Zn}_{0.9}\text{Co}_{0.1}(\text{CF}_3\text{-Im})_2$ decreases, until three minutes of milling time, where no crystalline phase is present any longer. From 5 min on the crystallization of qtz- $\text{Zn}_{0.9}\text{Co}_{0.1}(\text{CF}_3\text{-Im})_2$ begins, visible by the rising of its (100) reflection. The single product's maximum intensity is reached at 6.5 min, and no further changes in sample composition can be detected; thus, full conversion is reached.

As the DMF LAG conditions produce the pure SOD-polymorph of $\text{Zn}_{0.9}\text{Co}_{0.1}(\text{CF}_3\text{-Im})_2$ we also investigated the formation process by *in-situ* XRD. In a first phase until 30 s milling time, only the starting materials can be observed. In the second phase, their reflection intensities rise, as the milling process provides more powder into the beam. Furthermore, the (110) reflection of SOD- $\text{Zn}_{0.9}\text{Co}_{0.1}(\text{CF}_3\text{-Im})_2$ appears, and its intensity rises until 1 min milling time, where it reaches a first plateau. The following phase is characterized by the gradual decrease of starting materials reflections and increase of the reflections of SOD- $\text{Zn}_{0.9}\text{Co}_{0.1}(\text{CF}_3\text{-Im})_2$. After 6 min milling time, all starting materials reflections are disappeared, and after 7 min the (100) reflection of SOD- $\text{Zn}_{0.9}\text{Co}_{0.1}(\text{CF}_3\text{-Im})_2$ plateaus a second time. This indicates the completion of the reaction, as no further changes, the conversion into the qtz-polymorph, can be observed (**Figure 7**).

Carbonization of ZIFs is known as a method to produce nitrogen, and metal-doped carbon material (NMC) that can be applied is ORR electrocatalysis. The herein presented MOFs

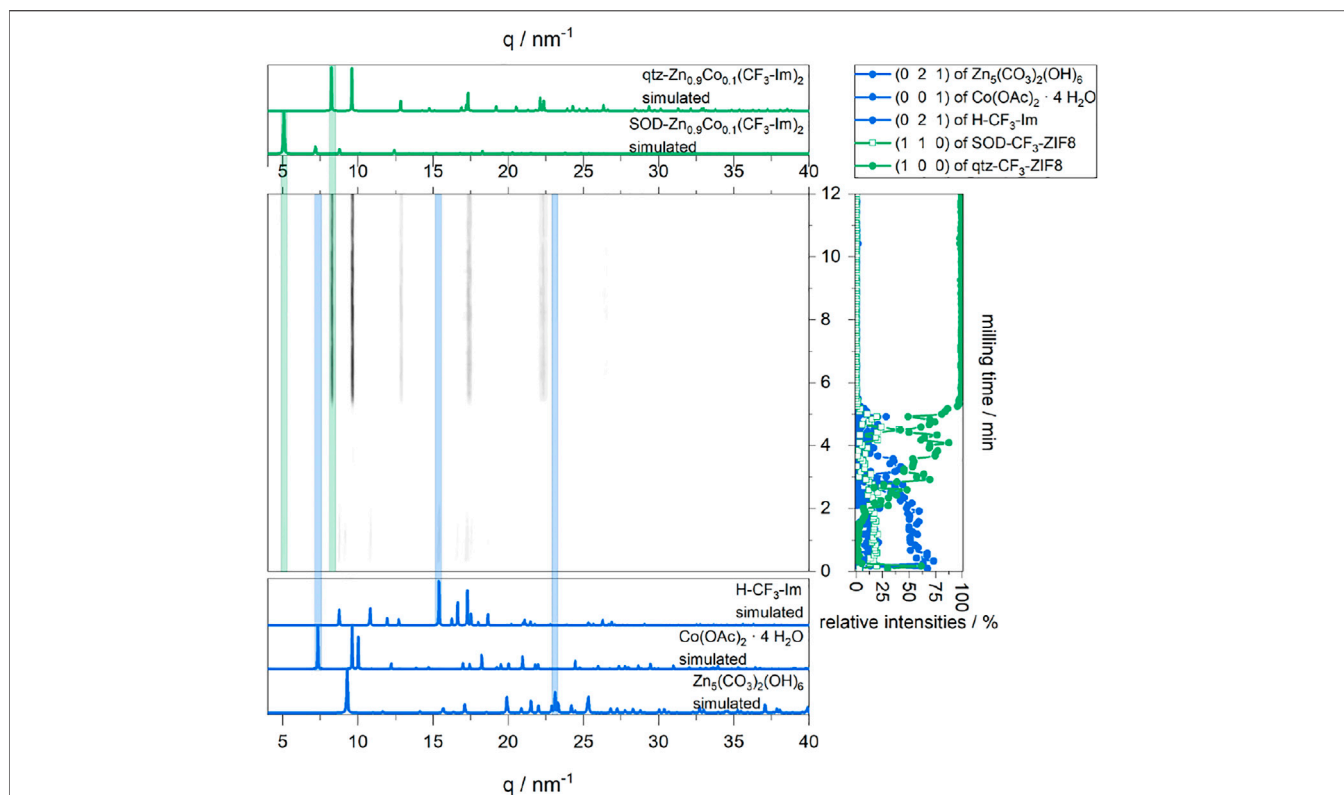


FIGURE 6 | *In situ* XRD plot of the formation of $\text{qtz-Zn}_{0.9}\text{Co}_{0.1}(\text{CF}_3\text{-Im})_2$ (center). For comparison, the simulated XRD patterns of starting materials (blue, bottom) and the products (green, top) are shown. The intensities of chosen reflections of the present phases are plotted on the right.

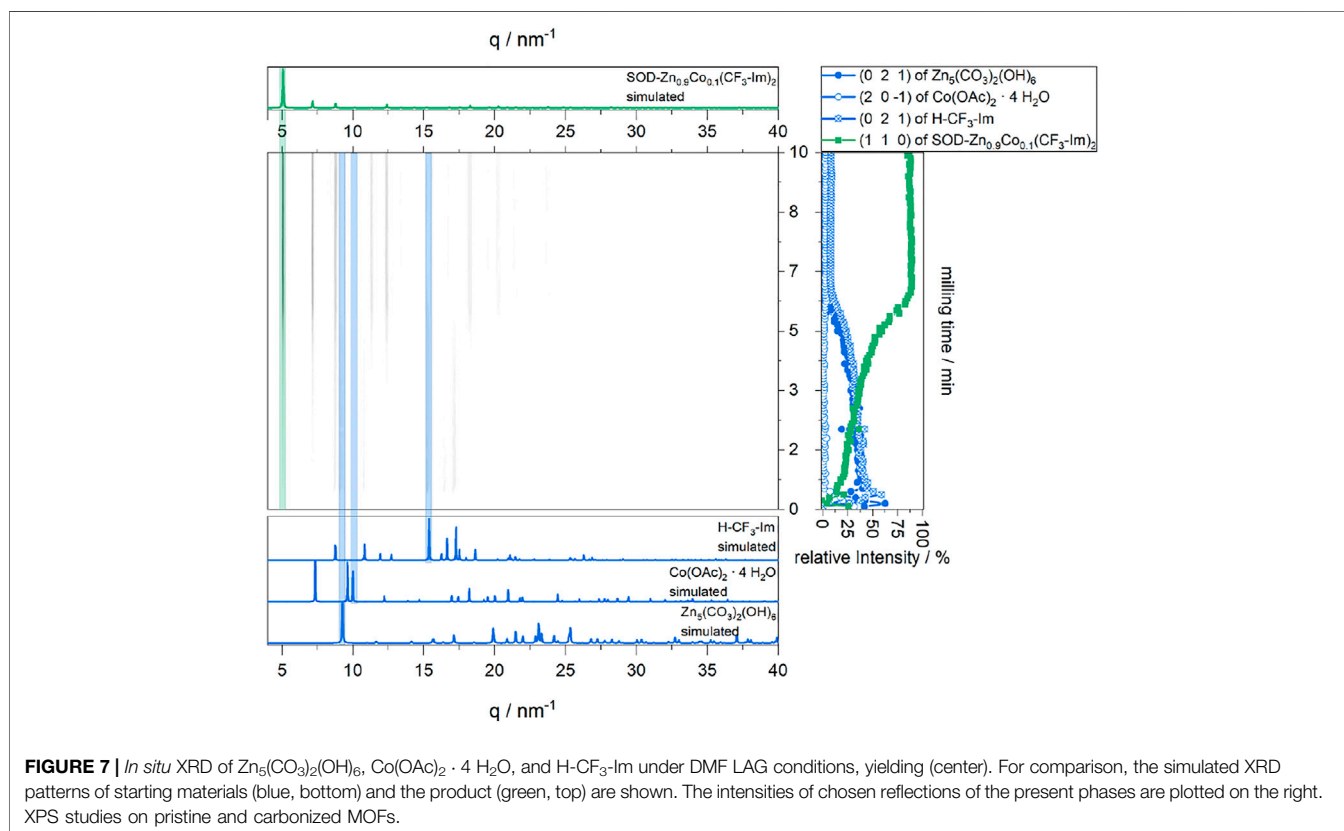
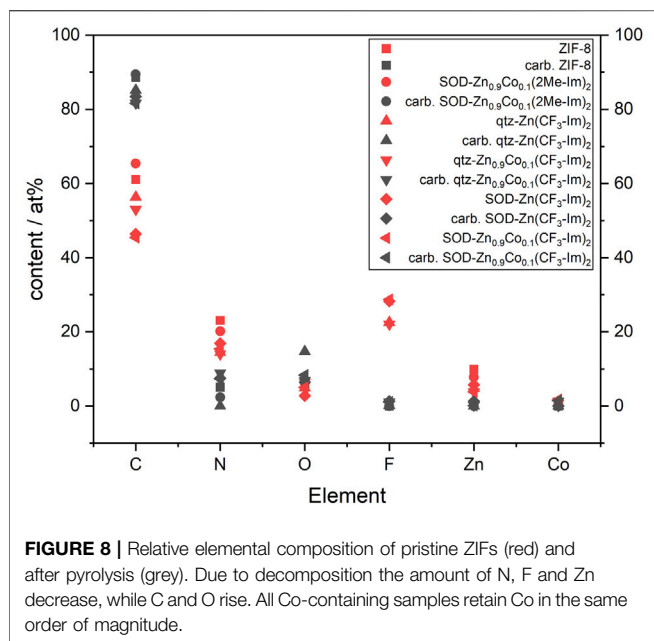


FIGURE 7 | *In situ* XRD of $\text{Zn}_5(\text{CO}_3)_2(\text{OH})_6$, $\text{Co}(\text{OAc})_2 \cdot 4 \text{H}_2\text{O}$, and $\text{H-CF}_3\text{-Im}$ under DMF LAG conditions, yielding (center). For comparison, the simulated XRD patterns of starting materials (blue, bottom) and the product (green, top) are shown. The intensities of chosen reflections of the present phases are plotted on the right. XPS studies on pristine and carbonized MOFs.



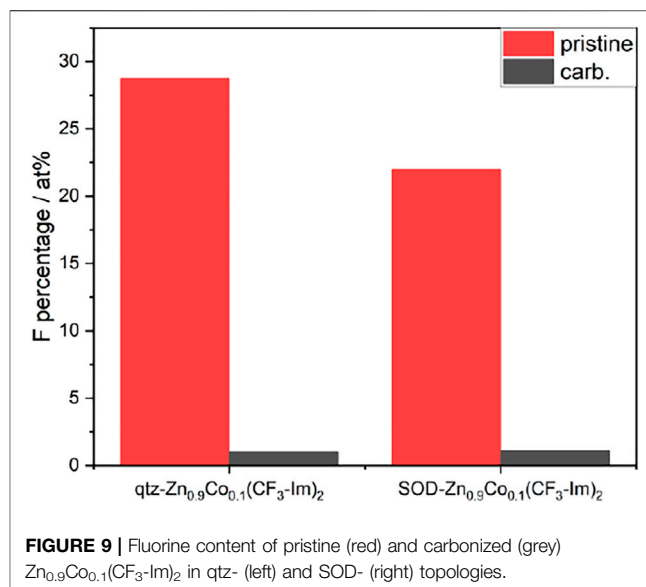
were therefore carbonized in a thermoscale with literature-known parameters. The samples are heated under a nitrogen atmosphere from room temperature to 900°C, where they are kept for 1 h, followed by a natural cool-down. *Ex situ* XPS was performed at the pristine MOFs and the pyrolysis products to obtain the elemental composition. As a surface-sensitive technique, XPS provides information about the outermost 10 nm of the samples. As a clear trend, it could be found that the amounts of nitrogen, fluorine, and zinc decrease, most likely due to these elements leaving by decomposition processes of the materials. As a direct consequence, the relative amount of carbon and oxygen rises. All Co-containing samples retain it in the same order of magnitude (Figure 8, 9).

The data of the fluorinated samples show for the carbonized materials the presence of two types of fluorine, metal-bound inorganic fluorine, and carbon-bound organic fluorine. In the carbonized $\text{Zn}_{0.9}\text{Co}_{0.1}(\text{CF}_3\text{-Im})_2$, the organic fluorine outweighs the inorganic with a ratio of 9:1.

The high-resolution spectra of Co2p photoelectron show a Co $2p_{3/2}$ peak at 780.5 eV and the satellite structure typical for Co^{2+} (Biesinger et al., 2011). For Zn, the Zn $2p_{3/2}$ peak at 1,022 eV was observed, which can be explained with bivalent Zn (Biesinger et al., 2010). For the pyrolyzed samples, some graphitization was observed indicated by the appearance of the typical shake up peak related to the $\pi \rightarrow \pi^*$ transition at 292 eV (see Supplementary Figures S9–S11).

Electrochemical Investigations, Oxygen Reduction Reaction Catalysis

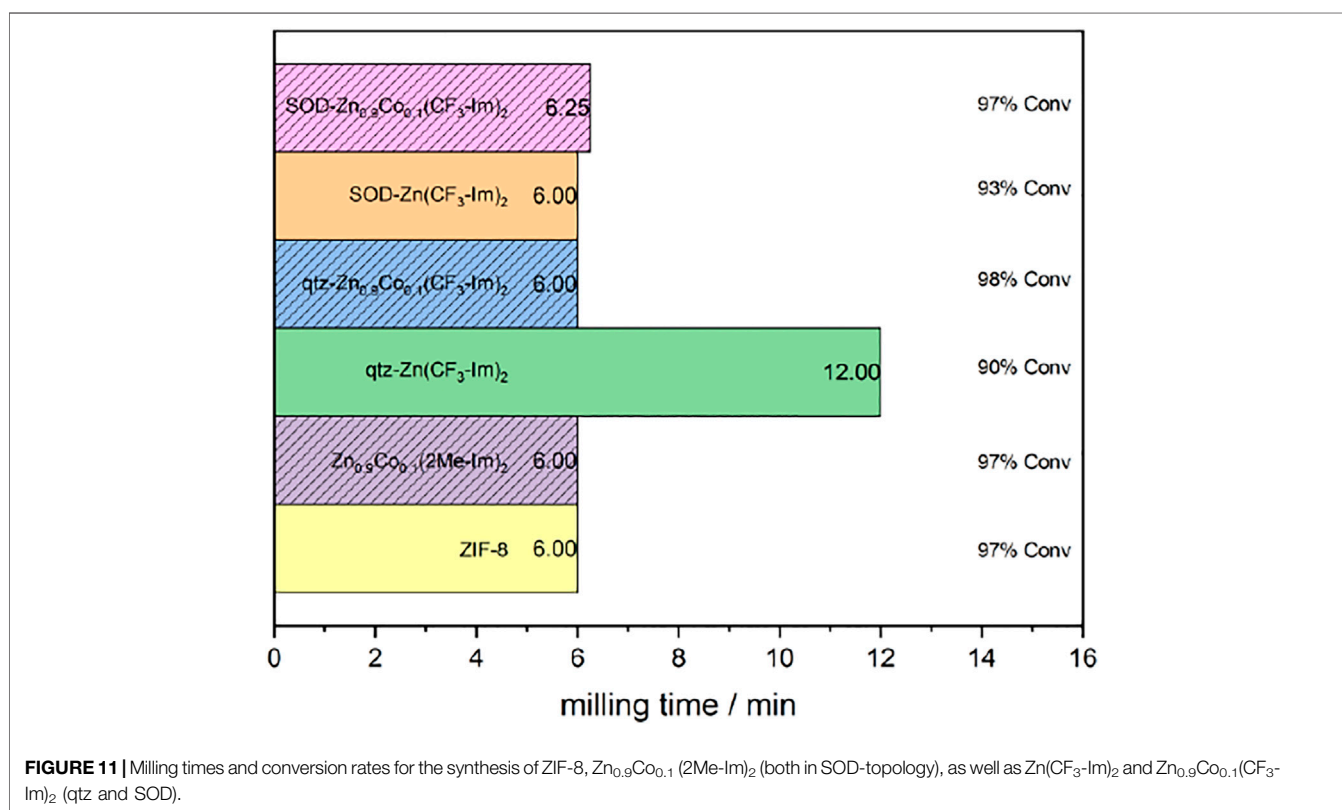
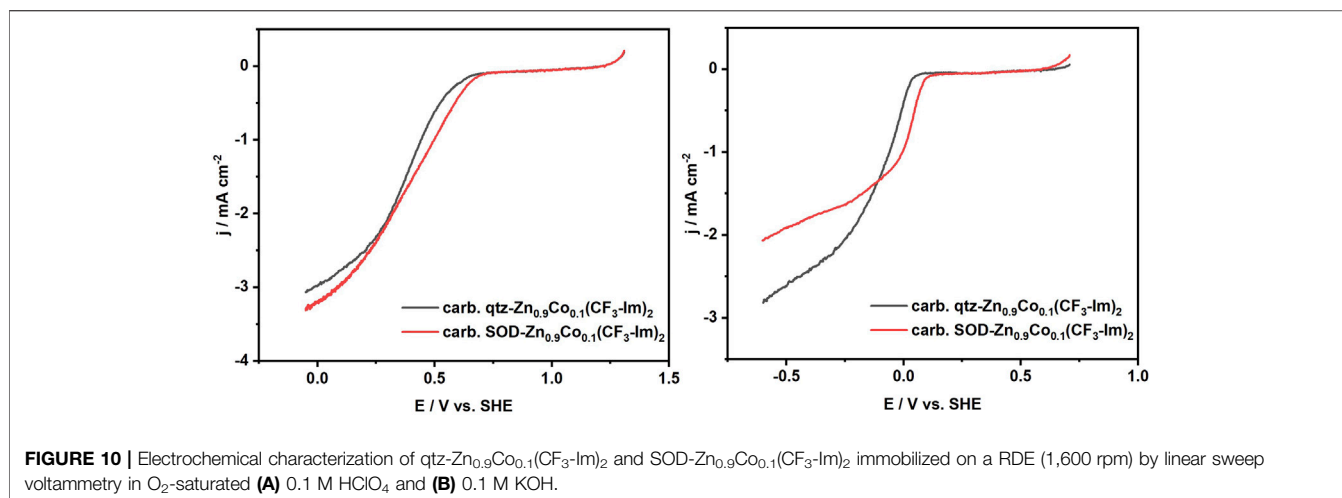
The performance of the ORR of pyrolyzed $\text{qtz-Zn}_{0.9}\text{Co}_{0.1}(\text{CF}_3\text{-Im})_2$ and $\text{SOD-Zn}_{0.9}\text{Co}_{0.1}(\text{CF}_3\text{-Im})_2$ was evaluated using the RDE. Figure 10 presents the ORR polarization curves measured



in O_2 -saturated 0.1 M KOH and 0.1 M HClO_4 electrolytes. In HClO_4 , both pyrolyzed Co-doped ZIFs exhibit a similar ORR activity with an onset potential of 0.67 V versus SHE for pyrolyzed $\text{qtz-Zn}_{0.9}\text{Co}_{0.1}(\text{CF}_3\text{-Im})_2$ and a higher onset potential of 0.70 versus SHE for pyrolyzed $\text{SOD-Zn}_{0.9}\text{Co}_{0.1}(\text{CF}_3\text{-Im})_2$ (Figure 10A). The half-wave potential gap between them was 22 mV, revealing a slightly higher activity of pyrolyzed $\text{SOD-Zn}_{0.9}\text{Co}_{0.1}(\text{CF}_3\text{-Im})_2$. In 0.1 M KOH, the pyrolyzed $\text{SOD-Zn}_{0.9}\text{Co}_{0.1}(\text{CF}_3\text{-Im})_2$ shows again a better activity toward the ORR in comparison to pyrolyzed $\text{qtz-Zn}_{0.9}\text{Co}_{0.1}(\text{CF}_3\text{-Im})_2$. The onset potential of pyrolyzed $\text{SOD-Zn}_{0.9}\text{Co}_{0.1}(\text{CF}_3\text{-Im})_2$ was found to be 0.12 V versus SHE with a half-wave potential of 0.0 V, whereas pyrolyzed $\text{SOD-Zn}_{0.9}\text{Co}_{0.1}(\text{CF}_3\text{-Im})_2$ exhibits a lower onset potential of 0.06 V versus SHE with a half-wave potential of -0.11 V. The half-wave potential gap between both systems was 0.10 mV. Furthermore, ORR polarization curves were measured under different rotation speeds and are presented in Supplementary Figure S8. The electrocatalytic activity in O_2 -saturated electrolytes was decreasing with the decrease in rotation rate, whereas almost no activity was observed in N_2 -saturated electrolytes. Our results indicate that both materials show electrocatalytic activity for ORR; however, no significant performance improvement was evident, depending on the polymorph of $\text{Zn}_{0.9}\text{Co}_{0.1}(\text{CF}_3\text{-Im})_2$ precursor.

Summary

In this work, we present the synthesis of the first $\text{Zn}_{0.9}\text{Co}_{0.1}(\text{CF}_3\text{-Im})_2$ frameworks by ball milling. Optimizing the grinding parameters allowed us to selectively produce polymorphs of $\text{Zn}_{0.9}\text{Co}_{0.1}(\text{CF}_3\text{-Im})_2$. Moreover, the formation was monitored *in situ* by synchrotron XRD measurements along with the formation of ZIF-8, $\text{Zn}_{0.9}\text{Co}_{0.1}(2\text{Me-Im})_2$, and $\text{Zn}(\text{CF}_3\text{-Im})_2$ frameworks. In Figure 11, a summary of milling times and conversion rates for the synthesis of ZIF-8, $\text{Zn}_{0.9}\text{Co}_{0.1}(2\text{Me-Im})_2$, and $\text{Zn}(\text{CF}_3\text{-Im})_2$ and $\text{Zn}_{0.9}\text{Co}_{0.1}(\text{CF}_3\text{-Im})_2$ (both in qtz-



and SOD-topologies, respectively) is given. The data showed for all the reactions one-step transformations from starting materials into products.

Furthermore, we investigated the chemical composition after carbonization of the prepared ZIFs, finding residue fluorine, mostly of organic nature. The pyrolyzed Zn_{0.9}Co_{0.1}(CF₃-Im)₂, both in qtz and SOD topology, was successfully used as ORR electrocatalysts in acidic and alkaline media. However, no significant differences in ORR activity for both polymorphs of pyrolyzed Zn_{0.9}Co_{0.1}(CF₃-Im)₂ could be observed.

DATA AVAILABILITY STATEMENT

The original contributions presented in the study are included in the article/Supplementary Material, further inquiries can be directed to the corresponding author.

AUTHOR CONTRIBUTIONS

This study was designed and supported by CR and FE. MR performed the synthesis and XRD analyses. MG and JW

contributed electrochemical measurements. JR performed XPS measurements. MR and FE wrote the original draft, viewed, and edited the manuscript. All authors reviewed and edited the manuscript. All authors have contributed to the work and approved the final version of the manuscript.

FUNDING

Gefördert durch die Deutsche Forschungsgemeinschaft (DFG)—Projektnummer 387284271—SFB 1349. Funded by the Deutsche Forschungsgemeinschaft (DFG, German Research Foundation)—Project-ID 387284271—SFB 1349.

REFERENCES

- Arhangelskis, M., Katsenis, A. D., Novendra, N., Akimbekov, Z., Gandrath, D., Marrett, J. M., et al. (2019). Theoretical Prediction and Experimental Evaluation of Topological Landscape and Thermodynamic Stability of a Fluorinated Zeolitic Imidazolate Framework. *Chem. Mater.* 31 (10), 3777–3783. doi:10.1021/acs.chemmater.9b00994
- Batzdorf, L., Fischer, F., Wilke, M., Wenzel, K.-J., and Emmerling, F. (2015). Direct *In Situ* Investigation of Milling Reactions Using Combined X-ray Diffraction and Raman Spectroscopy. *Angew. Chem. Int. Ed.* 54 (6), 1799–1802. doi:10.1002/anie.201409834
- Benecke, G., Wagermaier, W., Li, C., Schwartzkopf, M., Flucke, G., Hoerth, R., et al. (2014). A Customizable Software for Fast Reduction and Analysis of Large X-ray Scattering Data Sets: Applications of the newDPDAK package to Small-Angle X-ray Scattering and Grazing-Incidence Small-Angle X-ray Scattering. *J. Appl. Cryst.* 47 (Pt 5), 1797–1803. doi:10.1107/S1600576714019773
- Biesinger, M. C., Lau, L. W. M., Gerson, A. R., and Smart, R. S. C. (2010). Resolving Surface Chemical States in XPS Analysis of First Row Transition Metals, Oxides and Hydroxides: Sc, Ti, V, Cu and Zn. *Appl. Surf. Sci.* 257 (3), 887–898. doi:10.1016/j.apsusc.2010.07.086
- Biesinger, M. C., Payne, B. P., Grosvenor, A. P., Lau, L. W. M., Gerson, A. R., and Smart, R. S. C. (2011). Resolving Surface Chemical States in XPS Analysis of First Row Transition Metals, Oxides and Hydroxides: Cr, Mn, Fe, Co and Ni. *Appl. Surf. Sci.* 257 (7), 2717–2730. doi:10.1016/j.apsusc.2010.10.051
- Brunauer, S., Emmett, P. H., and Teller, E. (1938). Adsorption of Gases in Multimolecular Layers. *J. Am. Chem. Soc.* 60(2), 309–319. doi:10.1021/ja01269a023
- Bux, H., Liang, F., Li, Y., Cravillon, J., Wiebcke, M., and Caro, J. (2009). Zeolitic Imidazolate Framework Membrane with Molecular Sieving Properties by Microwave-Assisted Solvothermal Synthesis. *J. Am. Chem. Soc.* 131 (44), 16000–16001. doi:10.1021/ja907359t
- Chao, S., Bai, Z., Cui, Q., Yan, H., Wang, K., and Yang, L. (2015). Hollowed-out Octahedral Co/N-Codoped Carbon as a Highly Efficient Non-precious Metal Catalyst for Oxygen Reduction Reaction. *Carbon* 82, 77–86. doi:10.1016/j.carbon.2014.10.034
- Chapartegui-Arias, A., Villajos, J. A., Myxa, A., Beyer, S., Falkenhagen, J., Schneider, R. J., et al. (2019). Covalently Fluorophore-Functionalized ZIF-8 Colloidal Particles as a Sensing Platform for Endocrine-Disrupting Chemicals Such as Phthalates Plasticizers. *ACS Omega* 4 (17), 17090–17097. doi:10.1021/acsomega.9b01051
- Chen, D., Zhao, J., Zhang, P., and Dai, S. (2019). Mechanochemical Synthesis of Metal-Organic Frameworks. *Polyhedron* 162, 59–64. doi:10.1016/j.poly.2019.01.024
- Chen, Y.-Z., Wang, C., Wu, Z.-Y., Xiong, Y., Xu, Q., Yu, S.-H., et al. (2015). From Bimetallic Metal-Organic Framework to Porous Carbon: High Surface Area and Multicomponent Active Dopants for Excellent Electrocatalysis. *Adv. Mater.* 27 (34), 5010–5016. doi:10.1002/adma.201502315

ACKNOWLEDGMENTS

We thank BESSY II for beamtime allocation and the Deutsche Forschungsgemeinschaft for funding. Further thanks go to S. Reinsch for DTA-TG analysis, to C. Prinz for measuring TEM and EDS, and A. Zimathies for measuring N₂-sorption and calculation BET-surface areas of our samples.

SUPPLEMENTARY MATERIAL

The Supplementary Material for this article can be found online at: <https://www.frontiersin.org/articles/10.3389/fchem.2022.840758/full#supplementary-material>

- Cheplakova, A. M., Kovalenko, K. A., Samsonenko, D. G., Lazarenko, V. A., Khrustalev, V. N., Vinogradov, A. S., et al. (2018). Metal-organic Frameworks Based on Octafluorobiphenyl-4,4'-Dicarboxylate: Synthesis, crystal Structure, and Surface Functionality. *Dalton Trans.* 47 (10), 3283–3297. doi:10.1039/c7dt04566b
- Cravillon, J., Münzer, S., Lohmeier, S.-J., Feldhoff, A., Huber, K., and Wiebcke, M. (2009). Rapid Room-Temperature Synthesis and Characterization of Nanocrystals of a Prototypical Zeolitic Imidazolate Framework. *Chem. Mater.* 21 (8), 1410–1412. doi:10.1021/cm900166h
- Eddaoudi, M., Kim, J., Rosi, N., Vodak, D., Wachter, J., O'Keeffe, M., et al. (2002). Systematic Design of Pore Size and Functionality in Isoreticular MOFs and Their Application in Methane Storage. *Science* 295 (5554), 469–472. doi:10.1126/science.1067208
- Evers, M. V., Bernal, M., Roldan Cuenya, B., and Tschulik, K. (2019). Piece by Piece-Electrochemical Synthesis of Individual Nanoparticles and Their Performance in ORR Electrocatalysis. *Angew. Chem. Int. Ed.* 58 (24), 8221–8225. doi:10.1002/anie.201813993
- Farrusseng, D., Aguado, S., and Pinel, C. (2009). Metal-organic Frameworks: Opportunities for Catalysis. *Angew. Chem. Int. Ed.* 48 (41), 7502–7513. doi:10.1002/anie.200806063
- Fršić, T., Reid, D. G., Halasz, I., Stein, R. S., Dinnebier, R. E., and Duer, M. J. (2010). Ion- and Liquid-Assisted Grinding: Improved Mechanochemical Synthesis of Metal-Organic Frameworks Reveals Salt Inclusion and Anion Templating. *Angew. Chem. Int. Edition* 49 (4), 712–715. doi:10.1002/anie.200906583
- Gasteiger, H. A., Kocha, S. S., Sompalli, B., and Wagner, F. T. (2005). Activity Benchmarks and Requirements for Pt, Pt-alloy, and Non-pt Oxygen Reduction Catalysts for PEMFCs. *Appl. Catal. B: Environ.* 56 (1-2), 9–35. doi:10.1016/j.apcatb.2004.06.021
- Hao, J., Stavljenić Milašin, I., Batu Eken, Z., Mravak-Stipetic, M., Pavelić, K., and Ozer, F. (2021). Effects of Zeolite as a Drug Delivery System on Cancer Therapy: A Systematic Review. *Molecules* 26 (20), 6196. doi:10.3390/molecules26206196
- Hu, L., Chen, L., Peng, X., Zhang, J., Mo, X., Liu, Y., et al. (2020). Bifunctional Metal-Doped ZIF-8: A Highly Efficient Catalyst for the Synthesis of Cyclic Carbonates from CO₂ Cycloaddition. *Microporous Mesoporous Mater.* 299, 110123. doi:10.1016/j.micromeso.2020.110123
- Huang, X.-C., Lin, Y.-Y., Zhang, J.-P., and Chen, X.-M. (2006). Ligand-directed Strategy for Zeolite-type Metal-Organic Frameworks: Zinc(II) Imidazolates with Unusual Zeolitic Topologies. *Angew. Chem. Int. Ed.* 45 (10), 1557–1559. doi:10.1002/anie.200503778
- Iacomini, P., and Maurin, G. (2021). ResponZIF Structures: Zeolitic Imidazolate Frameworks as Stimuli-Responsive Materials. *ACS Appl. Mater. Inter.* 13 (43), 50602–50642. doi:10.1021/acsaami.1c12403
- Ibrahim, M., Sabouni, R., and Hussein, G. (2017). Anti-cancer Drug Delivery Using Metal Organic Frameworks (MOFs). *Cmc* 24 (2), 193–214. doi:10.2174/0929867323666160926151216
- Imawaka, K., Sugita, M., Takekaki, T., and Tanaka, S. (2019). Mechanochemical Synthesis of Bimetallic CoZn-ZIFs with Sodalite Structure. *Polyhedron* 158, 290–295. doi:10.1016/j.poly.2018.11.018

- Jiang, A., Chen, J., Liu, S., Wang, Z., Li, Q., Xia, D., et al. (2021). Intermetallic Rhodium Alloy Nanoparticles for Electrocatalysis. *ACS Appl. Nano Mater.* 4, 13716–13723. doi:10.1021/acsnm.1c03128
- Kang, S.-F., and Chang, H.-M. (1997). Coagulation of Textile Secondary Effluents with Fenton's Reagent. *Water Sci. Technol.* 36(12), 215–222. doi:10.1016/S0273-1223(97)00707-5
- Kaur, G., Rai, R. K., Tyagi, D., Yao, X., Li, P.-Z., Yang, X.-C., et al. (2016). Room-temperature Synthesis of Bimetallic Co-zn Based Zeolitic Imidazolate Frameworks in Water for Enhanced CO₂ and H₂ Uptakes. *J. Mater. Chem. A.* 4 (39), 14932–14938. doi:10.1039/c6ta04342a
- Keskin, S., van Heest, T. M., and Sholl, D. S. (2010). Can Metal-Organic Framework Materials Play a Useful Role in Large-Scale Carbon Dioxide Separations? *ChemSusChem* 3 (8), 879–891. doi:10.1002/cssc.201000114
- Klimakow, M., Klobes, P., Thünemann, A. F., Rademann, K., and Emmerling, F. (2010). Mechanochemical Synthesis of Metal–Organic Frameworks: A Fast and Facile Approach toward Quantitative Yields and High Specific Surface Areas. *Chem. Mater.* 22 (18), 5216–5221. doi:10.1021/cm1012119
- Kocha, S. S., Shinozaki, K., Zack, J. W., Myers, D. J., Kariuki, N. N., Nowicki, T., et al. (2017). Best Practices and Testing Protocols for Benchmarking ORR Activities of Fuel Cell Electrocatalysts Using Rotating Disk Electrode. *Electrocatalysis* 8 (4), 366–374. doi:10.1007/s12678-017-0378-6
- Kukkar, P., Kim, K.-H., Kukkar, D., and Singh, P. (2021). Recent Advances in the Synthesis Techniques for Zeolitic Imidazolate Frameworks and Their Sensing Applications. *Coord. Chem. Rev.* 446, 214109. doi:10.1016/j.ccr.2021.214109
- Lampronti, G. I., Michalchuk, A. A. L., Mazzeo, P. P., Belenguer, A. M., Sanders, J. K. M., Bacchi, A., et al. (2021). Changing the Game of Time Resolved X-ray Diffraction on the Mechanochemistry Playground by Downsizing. *Nat. Commun.* 12 (1), 6134. doi:10.1038/s41467-021-26264-1
- Li, X., Jiang, Q., Dou, S., Deng, L., Huo, J., and Wang, S. (2016). ZIF-67-derived Co-NC@CoP-NC Nanopolyhedra as an Efficient Bifunctional Oxygen Electrocatalyst. *J. Mater. Chem. A.* 4 (41), 15836–15840. doi:10.1039/c6ta06434e
- Lv, Y., Yang, L., and Cao, D. (2017). Nitrogen and Fluorine-Codoped Porous Carbons as Efficient Metal-free Electrocatalysts for Oxygen Reduction Reaction in Fuel Cells. *ACS Appl. Mater. Inter.* 9 (38), 32859–32867. doi:10.1021/acsmi.7b11371
- Ma, S., Goenaga, G. A., Call, A. V., and Liu, D.-J. (2011). Cobalt Imidazolate Framework as Precursor for Oxygen Reduction Reaction Electrocatalysts. *Chem. Eur. J.* 17 (7), 2063–2067. doi:10.1002/chem.201003080
- Macrae, C. F., Sovago, I., Cottrell, S. J., Galek, P. T. A., McCabe, P., Pidcock, E., et al. (2020). Mercury 4.0: from Visualization to Analysis, Design and Prediction. *J. Appl. Cryst.* 53 (Pt 1), 226–235. doi:10.1107/S1600576719014092
- Martinez Joaristi, A., Juan-Alcañiz, J., Serra-Crespo, P., Kapteijn, F., and Gascon, J. (2012). Electrochemical Synthesis of Some Archetypical Zn²⁺, Cu²⁺, and Al³⁺ Metal Organic Frameworks. *Cryst. Growth Des.* 12 (7), 3489–3498. doi:10.1021/cg300552w
- Masa, J., Zhao, A., Xia, W., Muhler, M., and Schuhmann, W. (2014). Metal-free Catalysts for Oxygen Reduction in Alkaline Electrolytes: Influence of the Presence of Co, Fe, Mn and Ni Inclusions. *Electrochimica Acta* 128, 271–278. doi:10.1016/j.electacta.2013.11.026
- Michalchuk, A. A. L., Boldyreva, E. V., Belenguer, A. M., Emmerling, F., and Boldyrev, V. V. (2021). Tribochemistry, Mechanical Alloying, Mechanochemistry: What Is in a Name? *Front. Chem.* 9 (359), 685789. doi:10.3389/fchem.2021.685789
- Mondal, S. S., Hovestadt, M., Dey, S., Paula, C., Glomb, S., Kelling, A., et al. (2017). Synthesis of a Partially Fluorinated ZIF-8 Analog for Ethane/ethene Separation. *CrystEngComm* 19 (39), 5882–5891. doi:10.1039/c7ce01438d
- Nirosha Yalamandala, B., Shen, W. T., Min, S. H., Chiang, W. H., Chang, S. J., and Hu, S. H. (2021). Advances in Functional Metal-Organic Frameworks Based On-Demand Drug Delivery Systems for Tumor Therapeutics. *Adv. Nanobio Res.* 1 (8), 2100014. doi:10.1002/anbr.202100014
- Palaniselvam, T., Biswal, B. P., Banerjee, R., and Kurungot, S. (2013). Zeolitic Imidazolate Framework (ZIF)-derived, Hollow-Core, Nitrogen-Doped Carbon Nanostructures for Oxygen-Reduction Reactions in PEFCs. *Chem. Eur. J.* 19 (28), 9335–9342. doi:10.1002/chem.201300145
- Park, K. S., Ni, Z., Cote, A. P., Choi, J. Y., Huang, R., Uribe-Romo, F. J., et al. (2006). Exceptional Chemical and thermal Stability of Zeolitic Imidazolate Frameworks. *Proc. Natl. Acad. Sci.* 103 (27), 10186–10191. doi:10.1073/pnas.0602439103
- Peng, H., Liu, F., Liu, X., Liao, S., You, C., Tian, X., et al. (2014). Effect of Transition Metals on the Structure and Performance of the Doped Carbon Catalysts Derived from Polyaniline and Melamine for ORR Application. *ACS Catal.* 4 (10), 3797–3805. doi:10.1021/cs500744x
- Pichon, A., Lazuen-Garay, A., and James, S. L. (2006). Solvent-free Synthesis of a Microporous Metal-Organic Framework. *CrystEngComm* 8 (3), 211–214. doi:10.1039/b513750k
- Schröder, C. A., Baburin, I. A., van Wüllen, L., Wiebcke, M., and Leoni, S. (2013). Subtle Polymorphism of Zinc Imidazolate Frameworks: Temperature-dependent Ground States in the Energy Landscape Revealed by experiment and Theory. *CrystEngComm* 15 (20), 4036–4040. doi:10.1039/c2ce26045j
- Son, W.-J., Kim, J., Kim, J., and Ahn, W.-S. (2008). Sonochemical Synthesis of MOF-5. *Chem. Commun.* (47), 6336–6338. doi:10.1039/b814740j
- Szczęśniak, B., Borysiuk, S., Choma, J., and Jaroniec, M. (2020). Mechanochemical Synthesis of Highly Porous Materials. *Mater. Horiz.* 7 (6), 1457–1473. doi:10.1039/d0mh00081g
- Tanaka, S., Nagaoka, T., Yasuyoshi, A., Hasegawa, Y., and Denayer, J. F. M. (2017). Hierarchical Pore Development of ZIF-8 MOF by Simple Salt-Assisted Mechanochemistry. *Cryst. Growth Des.* 18 (1), 274–279. doi:10.1021/acs.cgd.7b01211
- Venna, S. R., Jasinski, J. B., and Carreon, M. A. (2010). Structural Evolution of Zeolitic Imidazolate Framework-8. *J. Am. Chem. Soc.* 132 (51), 18030–18033. doi:10.1021/ja109268m
- Walling, C. (2002). Fenton's Reagent Revisited. *Acc. Chem. Res.* 8 (4), 125–131. doi:10.1021/ar50088a003
- Wang, X., Fan, X., Lin, H., Fu, H., Wang, T., Zheng, J., et al. (2016). An Efficient Co-N-C Oxygen Reduction Catalyst with Highly Dispersed Co Sites Derived from a ZnCo Bimetallic Zeolitic Imidazolate Framework. *RSC Adv.* 6 (44), 37965–37973. doi:10.1039/c6ra04771h
- Wang, X., Zhou, J., Fu, H., Li, W., Fan, X., Xin, G., et al. (2014). MOF Derived Catalysts for Electrochemical Oxygen Reduction. *J. Mater. Chem. A.* 2 (34), 14064–14070. doi:10.1039/c4ta01506a
- Wu, J., and Yang, H. (2013). Platinum-based Oxygen Reduction Electrocatalysts. *Acc. Chem. Res.* 46 (8), 1848–1857. doi:10.1021/ar300359w
- Xia, W., Zhu, J., Guo, W., An, L., Xia, D., and Zou, R. (2014). Well-defined Carbon Polyhedrons Prepared from Nano Metal-Organic Frameworks for Oxygen Reduction. *J. Mater. Chem. A.* 2 (30), 11606–11613. doi:10.1039/c4ta01656d
- Yang, C., Kaipa, U., Mather, Q. Z., Wang, X., Nesterov, V., Venero, A. F., et al. (2011). Fluorous Metal-Organic Frameworks with superior Adsorption and Hydrophobic Properties toward Oil Spill Cleanup and Hydrocarbon Storage. *J. Am. Chem. Soc.* 133 (45), 18094–18097. doi:10.1021/ja208408n
- Yang, D.-A., Cho, H.-Y., Kim, J., Yang, S.-T., and Ahn, W.-S. (2012). CO₂ capture and Conversion Using Mg-MOF-74 Prepared by a Sonochemical Method. *Energy Environ. Sci.* 5 (4), 6465–6473. doi:10.1039/c1ee02234b
- You, B., Jiang, N., Sheng, M., Drisdell, W. S., Yano, J., and Sun, Y. (2015). Bimetal-Organic Framework Self-Adjusted Synthesis of Support-free Nonprecious Electrocatalysts for Efficient Oxygen Reduction. *ACS Catal.* 5 (12), 7068–7076. doi:10.1021/acscatal.5b02325
- Zhang, D.-S., Chang, Z., Li, Y.-F., Jiang, Z.-Y., Xuan, Z.-H., Zhang, Y.-H., et al. (2013). Fluorous Metal-Organic Frameworks with Enhanced Stability and High H₂/CO₂ Storage Capacities. *Sci. Rep.* 3 (1), 3312. doi:10.1038/srep03312
- Zhang, J., Tan, Y., and Song, W.-J. (2020). Zeolitic Imidazolate Frameworks for Use in Electrochemical and Optical Chemical Sensing and Biosensing: a Review. *Microchim Acta* 187 (4). doi:10.1007/s00604-020-4173-3
- Zhang, M., Dai, Y., Hu, J.-Y., Miao, S., and Xu, B.-Q. (2021). Solvothermal Synthesis of Nanostructured Pt₂Ni Tetrahedrons with Enhanced Platinum Utilization and Activity toward Oxygen Reduction Electrocatalysis. *J. Phys. Chem. C* 125, 27199–27206. doi:10.1021/acs.jpcc.1c07755
- Zhao, S., Yin, H., Du, L., He, L., Zhao, K., Chang, L., et al. (2014). Carbonized Nanoscale Metal-Organic Frameworks as High Performance Electrocatalyst for

Oxygen Reduction Reaction. *ACS Nano* 8 (12), 12660–12668. doi:10.1021/nn505582e

Conflict of Interest: The authors declare that the research was conducted in the absence of any commercial or financial relationships that could be construed as a potential conflict of interest.

The handling Editor declared a past co-authorship with one of the authors FE.

Publisher's Note: All claims expressed in this article are solely those of the authors and do not necessarily represent those of their affiliated organizations, or those of

the publisher, the editors and the reviewers. Any product that may be evaluated in this article, or claim that may be made by its manufacturer, is not guaranteed or endorsed by the publisher.

Copyright © 2022 Rautenberg, Gernhard, Radnik, Witt, Roth and Emmerling. This is an open-access article distributed under the terms of the Creative Commons Attribution License (CC BY). The use, distribution or reproduction in other forums is permitted, provided the original author(s) and the copyright owner(s) are credited and that the original publication in this journal is cited, in accordance with accepted academic practice. No use, distribution or reproduction is permitted which does not comply with these terms.